Drag forces of porous-medium acoustics

Steven R. Pride
Earth Resources Laboratory, Department of Earth, Atmospheric, and Planetary Sciences, Massachusetts Institute of Technology, 42 Carleton Street, Cambridge, Massachusetts 02142

Frank Dale Morgan and Anthony F. Gangi
Department of Geophysics, Texas A&M University, College Station, Texas 77843
(Received 24 June 1992; revised manuscript received 22 October 1992)

The drag forces controlling the amount of relative flow induced in a fluid-saturated porous material by a mechanical wave are modeled here from first principles. Specifically, analytical expressions for the drag are derived for material models that possess variable-width pores; i.e., pores that have widths that vary with distance along their axis. The dynamic (complex, frequency-dependent) permeability determined for such a variable-width pore model is compared to estimates made using the models of Johnson, Koplik, and Dashen (JKD) and of Biot. Both the JKD model and the Biot model underestimate the imaginary part of the dynamic permeability at low frequencies with the amount of discrepancy increasing with the severity of the convergent or divergent flow, i.e., increasing with the magnitude of the maximum pore-wall slope relative to the channel axis. It is shown how to modify the JKD model to obtain proper low-frequency behavior. It is also shown that a simple series sum of constant-width flow channels does a poor job in approximating the drag of a variable-width channel.

I. INTRODUCTION

This paper is concerned with modeling the fluid flow induced in a fluid-saturated porous material by a mechanical wave. The material type to be considered is characterized as having continuously distributed fluid and solid phases; i.e., it is assumed that no isolated pockets of one phase are completely surrounded by the other phase. One example of this material type would be a packing of solid grains. As a compressional wave propagates through such a material, it both generates a pressure gradient in the fluid phase and accelerates the solid framework of the material. These two forces drive an accelerated flow of fluid relative to the solid frame. For a shear wave, the relative flow is driven only by the acceleration of the frame. As the fluid flows, traction forces are set up on the fluid/solid interface that act to resist the flow. These traction forces are called "drag forces." The magnitude of the relative flow is determined by the balance between the driving forces of the wave, the drag forces, and the inertial forces. In past work, the drag forces have been modeled by assuming the pore space to consist of a collection of constant-width flow channels, i.e., flow channels whose widths do not vary with distance along their axis.[1-3] In this work, allowance is made for variable-width flow channels.

The mechanical waves considered here have wavelengths much larger than the grains and pores comprising the material. Therefore, the response of interest is that which has been averaged over volumes much larger than a characteristic pore size but smaller than the wavelengths. Upon carrying out such a volume average on the force balance equations obeyed by the fluid and solid phases of a porous material, Pride, Gangi, and Morgan[4] have obtained the following coupled equations of motion:

$$\rho_B \frac{\partial \dot{\bar{\mathbf{u}}}_s}{\partial t} = \nabla \cdot \bar{\tau}_B - \rho_f \frac{\partial \dot{\bar{\mathbf{w}}}}{\partial t}, \tag{1}$$

$$\frac{\rho_f}{\phi} \frac{\partial \dot{\bar{\mathbf{w}}}}{\partial t} - \mathbf{d} = -\nabla \bar{p}_f - \rho_f \frac{\partial \dot{\bar{\mathbf{u}}}_s}{\partial t}, \tag{2}$$

where $\mathbf{d}$ is the drag force defined by

$$\mathbf{d} = \frac{1}{V_f} \int_{S_w} \mathbf{n} \cdot \tau_f \, dS. \tag{3}$$

τ_f are the actual fluid stresses acting on the "wall" surface S_w that separates the fluid and solid phases within the averaging volume. V_f is the volume of fluid in the averaging volume. Equation (1) corresponds to a force balance on the bulk material, while Eq. (2) corresponds to a force balance on the fluid in relative motion. Overbars denote volume-averaged quantities. The average relative fluid velocity $\dot{\bar{\mathbf{w}}}$ is defined as $\dot{\bar{\mathbf{w}}} = \phi(\dot{\bar{\mathbf{u}}}_f - \dot{\bar{\mathbf{u}}}_s)$, where ϕ is porosity, $\dot{\bar{\mathbf{u}}}_f$ is the average fluid velocity, and $\dot{\bar{\mathbf{u}}}_s$ is the average solid velocity. $\bar{\tau}_B$ is the average stress tensor acting on the bulk material, ρ_B is the bulk density, $\bar{p}_f$ is the average fluid pressure, and ρ_f is the fluid density. For an isotropic porous material, the stresses are related to the strains by

$$\bar{\tau}_B = (K_G \nabla \cdot \bar{\mathbf{u}}_s + C \nabla \cdot \bar{\mathbf{w}})\mathbf{I} + G(\nabla \bar{\mathbf{u}}_s + \nabla \bar{\mathbf{u}}_s^{\,T} - \tfrac{2}{3} \nabla \cdot \bar{\mathbf{u}}_s I) \tag{4}$$

and

$$-\bar{p}_f = C \nabla \cdot \bar{\mathbf{u}}_s + M \nabla \cdot \bar{\mathbf{w}}. \tag{5}$$

K_G, C, M, and G are the four moduli of isotropic poroelasticity. The definitions of these moduli obtained by Pride, Gangi, and Morgan[4] using volume-averaging arguments are identical to those initially obtained by Biot and

Willis.[5] Once the drag vector $\mathbf{d}$ has been specified, Eqs. (1), (2), (4), and (5) (plus boundary conditions) form a complete description of isotropic porous-media dynamics and are consistent with Biot's[6,7] equations.

The objective of this paper is to evaluate the drag integral defined by Eq. (3) for specific pore models so that analytical expressions for $\mathbf{d}$ are obtained in the form

$$\mathbf{d}=-\gamma\frac{\rho_f}{\phi}\frac{\partial\dot{\bar{\mathbf{w}}}}{\partial t}. \tag{6}$$

In general, γ is an integrodifferential time operator (or, in the frequency domain, a complex frequency-dependent quantity). Equation (2) can then be written

$$\rho_E\frac{\partial\dot{\bar{\mathbf{w}}}}{\partial t}=-\nabla\bar{p}_f-\rho_f\frac{\partial\dot{\mathbf{u}}_s}{\partial t}, \tag{7}$$

where

$$\rho_E=(1+\gamma)\frac{\rho_f}{\phi} \tag{8}$$

is the effective fluid-density operator that controls the magnitude of the wave-induced relative flow. For time-harmonic $e^{i\omega t}$ behavior, ρ_E can be related to the so-called "dynamic permeability" $k(\omega)$ by

$$k(\omega)=\frac{\mu_f}{i\omega\rho_E(\omega)}, \tag{9}$$

where μ_f is the shear viscosity of the fluid. Such a substitution is seen to put Eq. (7) in the form of Darcy's law.

Jonson, Koplik, and Dashen[8] (to be referred to as "JKD") have provided an interesting model for $k(\omega)$ that can be expressed entirely in terms of three parameters. After defining how the average time-harmonic flow through a porous material behaves in the limit of both low frequencies (Darcy's law) and high frequencies (inviscid flow except for a thin viscous-boundary layer near the pore walls), JKD simply connect the two limits with a postulated function given by

$$\frac{k(\omega)}{k_0}=\left[\left[1+iP\frac{\omega}{\omega_0}\right]^{1/2}+i\frac{\omega}{\omega_0}\right]^{-1}. \tag{10}$$

The three parameters are the dc permeability k_0, the transition frequency ω_0 that separates viscous-force-dominated flow from inertial-force flow, and a pore geometry term P that JKD suggest is commonly equal to $\frac{1}{2}$ for many porous media. The JKD model defines ω_0 as

$$\omega_0=\frac{\mu_f\phi}{\rho_f\alpha_\infty k_0}, \tag{11}$$

where α_∞ is called the "tortuosity" and will be given an exact definition later. Brown[9] has shown that α_∞ can be equated to the electrical formation factor F (the ratio of the fluid electrical conductivity to the bulk electrical conductivity of the porous material) as $\alpha_\infty=F\phi$; however, this relation is only valid if the solid phase is nonconductive and if surface conductivity is negligible. The JKD model defines the geometry term P as

$$P=\frac{4\alpha_\infty k_0}{\Lambda^2\phi} \tag{12}$$

where Λ possesses the units of length and has a formal definition in terms of the velocity potential for time-harmonic, inviscid flow. $\Lambda/2$ may be interpreted, approximately, as the pore-volume to pore-surface ratio V_f/S_w; however, it is found in this work that simply taking $P=\frac{1}{2}$ is a much better approximation. The frequency dependence of the JKD model is nearly identical to that of a grouping of constant-width flow channels; however, it is simplified in analytic form.

Charlaix, Kushnick, and Stokes[10] have experimentally measured the dynamic permeability for samples of fused-glass beads and crushed glass. Their samples have porosities on the order of 50% and grain sizes ranging from 200 to 1000 μm. They obtain that Eq. (10) generally fits the data well; however, discrepancies occur for the imaginary part of $k(\omega)$ at frequencies $\omega<\omega_0$ with differences on the order of 35%. They determine the parameter P of Eq. (10) to be between 0.4 and 0.5 for their samples in agreement with JKD. Zhou and Sheng[11] have provided finite-element modeling of the dynamic permeability for a variety of specific pore models that possess variable-width flow channels. They also find the JKD model to be generally satisfactory with the only deviations from Eq. (10) occurring when the throat regions of the flow channels become "sharp;" i.e., when the slope of the channel walls relative to the channel axis significantly deviates from zero in the throat region. Discrepancies in these cases are again largest for the imaginary part of $k(\omega)$ at frequencies $\omega<\omega_0$. The discrepancies can be as large as 90% for some of their numerical simulations. The trend in both the studies of Zhou and Sheng[11] and Charlaix, Kushnick, and Stokes[12] is for the imaginary part of $k(\omega)$ to be underestimated by Eq. (10) when $\omega<\omega_0$.

The reason for the discrepancies is that JKD do not require the imaginary part of $k(\omega)$ to satisfy the exact frequency dependence in the limit of $\omega\ll\omega_0$. In this paper, the frequency-dependent flow properties of a variable-channel-width model are analytically solved for. It is also shown how to generalize the JKD model so that it contains the correct low-frequency behavior.

II. DRAG MODELING ASSUMPTIONS

To evaluate the drag force $\mathbf{d}$, the actual fluid stresses τ_f acting on the walls of a given porous medium model are required. These stresses are given by

$$\tau_f=-p_f\mathbf{I}+\kappa_f\nabla\cdot\dot{\mathbf{u}}_f\mathbf{I}+\mu_f(\nabla\dot{\mathbf{u}}_f+\nabla\dot{\mathbf{u}}_f^{\,T}-\tfrac{2}{3}\nabla\cdot\dot{\mathbf{u}}_f\mathbf{I}), \tag{13}$$

where p_f and $\dot{\mathbf{u}}_f$ are the actual (nonaveraged) thermodynamic fluid pressure and the fluid velocity. κ_f is the coefficient of bulk viscosity. To obtain p_f and $\dot{u}_f$, one must solve the equations of motion

$$\rho_f\left[\frac{\partial\dot{\mathbf{u}}_f}{\partial t}+\dot{\mathbf{u}}_f\cdot\nabla\dot{\mathbf{u}}_f\right]=\nabla\cdot\tau_f \tag{14}$$

subject to the continuity equation $[\partial\rho_f/\partial t=-\nabla\cdot(\rho_f\dot{\mathbf{u}}_f)]$ and the boundary conditions for a particular pore model.

In general, this is a rather intractable problem that can only be solved numerically. Fortunately, several assumptions can be made that greatly simplify the analysis. These assumptions will now be laid out.

A. Fluid incompressibility

In the local modeling of τ_f, it can assumed that the fluid responds incompressibility ($\nabla\cdot\dot{\mathbf{u}}_f \simeq 0$) so long as the wave frequencies are small enough that scattering from the grains of the material does not occur. Batchelor[12] estimates how much the fluid density changes due to time-harmonic shaking of an object whose size is of the order a (a can be interpreted to be a typical grain size). He obtains that if

$$\frac{f^2a^2}{c_f^2} \ll 1, \tag{15}$$

where f is frequency in cycles per second and c_f is the velocity of sound in the fluid, then density variations are negligible in the equations of motion and $\nabla\cdot\dot{\mathbf{u}}_f \simeq 0$. Since c_f is the order of typical wave speeds in porous materials (albeit usually two or three times smaller), it is seen that condition (15) is equivalent to the no-grain-scattering condition $\lambda \gg a$, where λ is the wavelength of the mechanical waves. It will be assumed throughout that condition (15) is satisfied.

B. Framework incompressibility

It is assumed that in the modeling of $\mathbf{d}$, the framework of grains, is rigidly accelerating. In other words, it is assumed that within an averaging volume (i) variations in the amount of wall-surface area S_w due to compressional stressing are negligible and (ii) spatial variations in the acceleration of the walls are negligible. It has already been assumed that linear stress-strain relations [as given by Eqs. (4) and (5)] govern the material response. Experimental evidence shows this to be the case if compressional-wave strains ϵ are less than 10^{-6}. If the wall-surface area S_w is expressed as $S_w = S_{w0} + \delta S_w$, where S_{w0} is the surface area in an averaging volume prior to stressing, then it is easily established that $|\delta S_w / S_{w0}| < \epsilon$. For example, if the pores are modeled as cylinders, then

$$|\delta S_w / S_{w0}| = \sqrt{1+\epsilon} - 1 < \epsilon \ .$$

Thus S_w may be replaced by S_{w0} in the drag integral with great accuracy and assumption (i) is satisfied. Assumption (ii) is also trivially satisfied because variations in the acceleration of the walls occur over distances associated with the wavelengths. If the averaging volume is assumed to be much smaller than the wavelengths, then the wall accelerations can be modeled as being constant within an averaging volume.

One additional consideration must be addressed. In granular materials, pore fluid may be present in the grain contact regions. It is the asperities on the grain surfaces that are in contact, so fluid may reside in the regions surrounding the asperity contacts. Although such regions contribute only minutely to the total porosity, they can have a significant effect on the overall compressibility of the material as discussed by Murphy, Winkler, and Kleinberg.[13] For small background stress levels prior to wave stressing, the grain-contact regions are "open" and are highly compliant. When such a granular material is compressed by a wave, a fluid pressure develops in the grain contacts that is much larger than the fluid pressure in the main pore volumes. A local flow of fluid from the grain contacts to the main pore volumes is induced that acts to equilibrate the fluid pressure imbalance. Such local flow can be roughly modeled as being radially symmetric about the center of each grain contact area and will, therefore, volume averaging to zero (i.e., it does not directly contribute to $\dot{\bar{\mathbf{w}}}$). By the same argument, such local flow will not contribute to the drag integral [Eq. (3)].

However, the local flow will tend to enhance slightly the macroscopic wavelength-scale pressure gradient in the main pore volumes. Such a pressure-gradient enhancement will relax (be reduced) when the wave periods become smaller than the amount of time it takes for the pressure equilibration between the contacts and the main pore volumes to occur. The material will effectively stiffen at such small wave periods. For the special case where $\dot{\bar{\mathbf{w}}} = \mathbf{0}$, Murphy, Winkler, and Kleinberg[13] have provided initial modeling of these effects and show how to allow for such "contact relaxations" by adding a complex, frequency-dependent term to the elastic constants K_G and G of Eq. (5). Generalizing their results to the case where $\dot{\bar{\mathbf{w}}} \neq \mathbf{0}$ is the subject of a future investigation. It is clear that when $\dot{\bar{\mathbf{w}}} \neq \mathbf{0}$, the contact relaxation will affect all four poroelastic moduli K_G, C, M, and G. In this work, it is simply assumed that variations in the macroscopic fluid-pressure gradients due to contact relaxation are allowed for in the stress-strain relations.

The only way that such local flow could affect the drag calculations of this paper is if the fluid being injected from the contacts into the main flow channels significantly altered the flow pattern in the main channels. However, the dominant contribution to the drag integral comes from the throat regions of the flow channels, while the local flow is being injected from the grain contacts, which are typically in the "calm" regions of the channels where little drag contribution is occurring. Such an effect is therefore ignored.

In conclusion, then, it may be assumed that the actual relative fluid flow $\mathbf{v}(\mathbf{r})$ within an averaging volume may be expressed as

$$\mathbf{v}(\mathbf{r}) = \dot{\mathbf{u}}_f(\mathbf{r}) - \dot{\bar{\mathbf{u}}}_s . \tag{16}$$

C. Ignoring the nonlinear convective acceleration

The force balance on the fluid within a flow channel may now be expressed as

$$\rho_f \left[\frac{\partial \mathbf{v}}{\partial t} + (\mathbf{v} + \dot{\tilde{\mathbf{u}}}_s) \cdot \nabla \mathbf{v} \right] = -\nabla p_f + \nabla \cdot \tau^D - \rho_f \frac{\partial \dot{\tilde{\mathbf{u}}}_s}{\partial t}, \quad (17)$$

where τ^D represents the "deviatoric" stress and is given by

$$\tau^D = \mu_f (\nabla \mathbf{v} + \nabla \mathbf{v}^T). \quad (18)$$

To arrive at this equation, both Eq. (16) and $\nabla \cdot \mathbf{v} = 0$ have been substituted into Eq. (14).

It would be convenient to ignore the convection term in Eq. (17). For relative flow induced in constant-width flow channels, the convection term is exactly zero; however, it is nonzero for relative flow in channels that possess a half-width function $h(z)$ that varies with distance z along the channel axis. If it can be shown that $\dot{\tilde{\mathbf{u}}}_s \cdot \nabla \mathbf{v}$ is negligible, then $\mathbf{v} \cdot \nabla \mathbf{v}$ will also be negligible because the induced relative flow $\mathbf{v}$ is smaller in magnitude than the wall velocity.

Two frequency domains control the nature of the relative flow. At sufficiently low frequencies, the viscous shear forces $\nabla \cdot \tau^D$ dominate the inertial forces $\rho_f \partial \mathbf{v} / \partial t$, while, at sufficiently high frequencies, $\rho_f \partial \mathbf{v} / \partial t$ dominates $\nabla \cdot \tau^D$. Therefore, for $\dot{\tilde{\mathbf{u}}}_s \cdot \nabla \mathbf{v}$ to be negligible, the Reynold's number

$$R \equiv |\rho_f \dot{\tilde{\mathbf{u}}}_s \cdot \nabla \mathbf{v}| / |\nabla \cdot \tau^D|$$

must be much less than one at low frequencies, while the Strouhal number

$$S \equiv |\dot{\tilde{\mathbf{u}}}_s \cdot \nabla \mathbf{v}| / |\partial \mathbf{v} / \partial t|$$

must be much less than one at high frequencies. It is straightforward to establish[4] the following estimates for S and R in a variable-width flow channel:

$$S \simeq \frac{1}{h_0} \left| \frac{dh}{dz} \right| \frac{\epsilon c}{\omega} \quad (19)$$

and

$$R \simeq \frac{\omega}{\omega_1} S, \quad (20)$$

where

$$\omega_1 = \frac{\mu_f}{\rho_f h_0^2}. \quad (21)$$

ω_1 is another expression [c.f., Eq. (11)] for the transition frequency separating the low- and high-frequency domains, c is the wave speed, ϵ is the wave strain, h_0 is the mean channel half width, and $|dh/dz|$ is a characteristic (i.e., flow-controlling) channel-wall or streamline slope. It is clear that both S and R tend to zero in the limit of high and low frequencies, respectively, as desired. At the transition frequency, S and R are given by

$$S = R = \frac{\epsilon h_0 \rho_f c}{\mu_f} \left| \frac{dh}{dz} \right|. \quad (22)$$

For water as the saturating fluid and a maximum allowed strain of 10^{-6} one obtains the geometric condition that

$$h_0 \left| \frac{dh}{dz} \right| \ll 100 \ (\mu\text{m}) \quad (23)$$

if the nonlinear convection terms are to be considered negligible. Since flow-controlling channel-wall slopes are likely to be characterized by $|dh/dz| \leq 1$, the condition simply becomes that $h_0 \ll 100$ μm, which is satisfied by many porous media of interest. It is assumed that condition (23) is satisfied.

D. Form drag and friction drag

Given the above assumptions, the drag vector may now be written as

$$\mathbf{d} = \mathbf{d}^{(\text{form})} + \mathbf{d}^{(\text{fric})}, \quad (24)$$

where

$$\mathbf{d}^{(\text{form})} = \frac{1}{V_f} \int_{S_w} -p_f \mathbf{n} \, dS' \quad (25)$$

and

$$\mathbf{d}^{(\text{fric})} = \frac{1}{V_f} \int_{S_w} \mu_f \mathbf{n} \cdot (\nabla \mathbf{v} + \nabla \mathbf{v}^T) dS'. \quad (26)$$

The equations satisfied by the relative velocity $\mathbf{v}$ and the fluid pressure p_f are the incompressibility condition $\nabla \cdot \mathbf{v} = 0$ and the equation of motion (the Navier-Stokes equation)

$$\rho_f \frac{\partial \mathbf{v}}{\partial t} = -\nabla p_f + \mu_f \nabla^2 \mathbf{v} - \rho_f \frac{\partial \dot{\tilde{\mathbf{u}}}_s}{\partial t}. \quad (27)$$

The separation into form drag and friction drag is made because the two have distinctly different character. The form drag depends strongly on the shape of the pore channels, this being significant when there are convergent or divergent, or tortuous, flow channels. It is largely (but not entirely) an inertial effect proportional to $\partial \dot{\tilde{\mathbf{w}}} / \partial t$. The friction drag, however, depends mainly on the smallest channel aperture, and is, as the name implies, largely (but not entirely) a frictional effect proportional to $\dot{\tilde{\mathbf{w}}}$. For time-harmonic motions, the two drags therefore have different frequency dependence. In particular, it should be noted that for constant-width flow channels, the normal to the walls is perpendicular to the average-flow direction and, therefore, the form drag provides no flow resistance. In a variable-width model, however, there is always a form-drag contribution with the contribution increasing with increasing slope of the channel walls.

III. THE VARIABLE-CHANNEL-WIDTH MODEL

In this section, the drag integrals will be determined for two-dimensional flow in channels possessing periodic and smooth variations in their half-width function $h(z)$. A typical channel cross section is depicted in Fig. 1. Cartesian coordinates (x,z) are employed. Only wall oscillations $\dot{\tilde{u}}_z$ and macroscopic pressure gradients $\partial \bar{p} / \partial z$ in

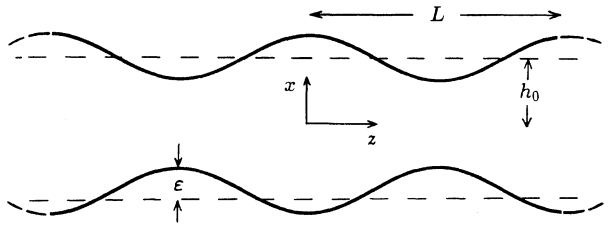

FIG. 1. A variable-width flow channel.

the z (axial) direction need be considered because the x components of these quantities do not generate drag. The subscript "f" referring to the fluid will be dropped henceforth. The channel periodicity may be expressed as $h(z)=h(z+L)$, where $h(z)$ is the half-width function, and it is further assumed that $L \gg h(z)$. L being significantly larger than $h(z)$ (say at least a factor of 4) will provide the basis for an analytical solution to the problem. Adjusting the results to accommodate flow in channels possessing circular cross sections will be briefly discussed in a later section.

A. Flow velocity and pressure determination

For time-harmonic stressing, the Navier-Stokes equation can be rewritten as

$$\left[\frac{\partial^2}{\partial z^2}+\frac{\partial^2}{\partial x^2}\right]v_z-i\xi^2 v_z=\frac{1}{\mu}\frac{\partial p}{\partial z}+i\xi^2\ddot{u}_z, \tag{28}$$

$$\left[\frac{\partial^2}{\partial z^2}+\frac{\partial^2}{\partial x^2}\right]v_x-i\xi^2 v_x=\frac{1}{\mu}\frac{\partial p}{\partial x}\ , \tag{29}$$

where

$$\xi=\sqrt{\omega\rho/\mu}. \tag{30}$$

The relative velocities v_x and v_z must also satisfy the incompressibility condition

$$\frac{\partial v_z}{\partial z}+\frac{\partial v_x}{\partial x}=0, \tag{31}$$

and the boundary and symmetry conditions

$$v_z(x=\pm h)=v_x(x=\pm h)=0, \tag{32}$$

$$v_x(x=0)=\frac{\partial v_z}{\partial x}(x=0)=0. \tag{33}$$

Analytical solutions to this differential problem are obtained if it is assumed that

$$\frac{\partial^2}{\partial z^2}\ll\frac{\partial^2}{\partial x^2} \tag{34}$$

[i.e., $h^2\ll(L/2)^2$]. A successive-approximation solution scheme begins by making the additional assumption that

$$\frac{\partial p}{\partial x}\ll\frac{\partial p}{\partial z} \tag{35}$$

(i.e., $|dh/dz|\ll 1$). Taking $\partial p/\partial x \ll \partial p/\partial z$ is equivalent to saying that $p(x,z)\simeq p(z)$ (i.e., variations in pressure across the channel are insignificant). That this is equivalent to the statement $|dh/dz|\simeq|v_x/v_z|\ll 1$ is easily determined from the Navier-Stokes equations. This condition will be relaxed through the successive-approximation scheme; however, condition (34) will not be relaxed and is the fundamental restriction on the geometry.

Given conditions (34) and (35), the governing equations become

$$\frac{\partial^2 v_z}{\partial x^2}-i\xi^2 v_z=\frac{1}{\mu}\frac{\partial p}{\partial z}+i\xi^2\ddot{u}_z \tag{36}$$

and

$$v_x=-\int^x\frac{\partial v_z}{\partial z}dx. \tag{37}$$

These equations, subject to the given boundary and symmetry conditions, can be solved with the result

$$v_z^{(1)}=\frac{Q_z^{(1)}}{h}F\left[1-\frac{\cosh i^{1/2}\xi x}{\cosh i^{1/2}\xi h}\right], \tag{38}$$

$$v_x^{(1)}=i\xi^2 Q_z^{(1)}h\frac{dh}{dz}G^2\left[\frac{x}{h}-\frac{\sinh i^{1/2}\xi x}{\sinh i^{1/2}\xi h}\right], \tag{39}$$

and

$$\frac{dp^{(1)}}{dz}=-i\xi^2\mu\left[\ddot{u}_z+\frac{Q_z^{(1)}}{h}F\right], \tag{40}$$

where the superscript (1) on the velocities and pressure means that this is the first-order approximation to the problem. F and G are auxiliary coefficients defined as

$$F=\frac{i^{1/2}\xi h}{i^{1/2}\xi h-\tanh i^{1/2}\xi h},$$
$$G=\frac{\tanh i^{1/2}\xi h}{i^{1/2}\xi h-\tanh i^{1/2}\xi h}, \tag{41}$$

while $Q_z^{(1)}$ is the volumetric flow-rate constant defined as

$$Q_z^{(1)}=\int_0^h v_z^{(1)}dx. \tag{42}$$

$Q_z^{(1)}$ therefore represents half the total volume of fluid fluxing axially through a cross-section of the channel per unit time and per unit length in the y direction. Since the fluid is incompressible, $Q_z^{(1)}$ must everywhere be constant.

To proceed to the next level of approximation, the neglected x component of the Navier-Stokes equation [Eq. (29)] is integrated so that pressure variations across the channel width are allowed for. This gives

$$p^{(2)}(x,z)=p^{(1)}(z)+\mu\frac{\partial v_x^{(1)}}{\partial x}\Bigg|_0^x-i\xi^2\mu\int_0^x v_x^{(1)}dx \tag{43}$$

$$=p^{(1)}(z)+\mu Q_z^{(1)}\xi^4\frac{dh}{dz}G^2\frac{x^2}{2}\ . \tag{44}$$

It is easily shown that the real part of G^2 is negative (at least for $\xi h<1$), which gives the intuitive result that in

converging portions of the channel ($dh/dz<0$) the pressure at the wall is greater than at the axis, while in diverging portions ($dh/dz>0$) the pressure at the wall is less than at the axis.

The updated pressure gradient is then given by

$$\frac{\partial p^{(2)}(x,z)}{\partial z}=\frac{\partial p^{(1)}(z)}{\partial z}+\mu Q_z^{(1)}\xi^4 H\frac{x^2}{2}, \tag{45}$$

where

$$H=\frac{\partial}{\partial z}\left[\frac{dh}{dz}G^2\right]. \tag{46}$$

Returning to Eq. (36) with this new pressure gradient allows v_z to be updated:

$$v_z^{(2)}=v_z^{(1)}+Q_z^{(1)}H\left[\left[1+\frac{i\xi^2x^2}{2}\right]-\left[1+\frac{i\xi^2h^2}{2}\right]\frac{\cosh i^{1/2}\xi x}{\cosh i^{1/2}\xi h}\right]. \tag{47}$$

From the continuity equation [Eq. (37)], v_x is updated,

$$v_x^{(2)}=v_x^{(1)}-Q_z^{(1)}\frac{\partial H}{\partial z}\left[\left[x+\frac{i\xi^2x^3}{6}\right]-\left[h+\frac{i\xi^2h^3}{6}\right]\frac{\sinh i^{1/2}\xi x}{\sinh i^{1/2}\xi h}\right], \tag{48}$$

and, finally, the flow-rate constant is updated,

$$Q_z^{(2)}=\int_0^h v_z^{(2)}dx=Q_z^{(1)}[1+hHJ], \tag{49}$$

where J is another auxiliary coefficient given by

$$J=\left[1+\frac{i\xi^2h^2}{6}\right]-\left[1+\frac{i\xi^2h^2}{2}\right]\frac{\tanh i^{1/2}\xi h}{i^{1/2}\xi h}. \tag{50}$$

The last step is to replace $Q_z^{(1)}$ by $Q_z^{(2)}/(1+hHJ)$ in the above expressions for $v_z^{(2)}$, $v_x^{(2)}$, and $p^{(2)}$, where $Q_z^{(2)}$ is now taken as the flow-rate constant. What Eq. (49) says is that, in reality, $Q_z^{(1)}$ as defined by Eq. (42) was not really a constant independent of z. Strictly speaking, this means that an additional term proportional to $\partial Q_z^{(1)}/\partial z$ should have been allowed for in the expression for $\partial p^{(2)}/\partial z$. If this additional term is carried through into the expression for $Q_z^{(2)}$, it is easily shown to be proportional to $|dh/dz|^4$. Since the other terms at this level of approximation are at most proportional to $|dh/dz|^2$, the process of taking $Q_z^{(1)}$ as constant until it is replaced at the end with Eq. (49) is therefore justified. Terms proportional to $|dh/dz|^4$ are allowed for at the next level of approximation.

The error in the first-order approximation is of $O(|dh/dz|^2)$, while the error in the second-order approximation is of $O(|dh/dz|^4)$. The process could clearly be continued *ad infinitum*, generating an infinite series so long as $|dh/dz|_{\max}<1$. For $|dh/dz|_{\max}>1$, the series would almost certainly diverge; however, the constraint of $|dh/dz|_{\max}<1$ seems reasonable for many porous materials. In practice, the successive-approximation scheme has not been taken further than the second-order results given above.

B. A flow-modeling example

Consider the simple pore model given by

$$h(z)=h_0+\varepsilon\cos\left[\frac{2\pi z}{L}\right]. \tag{51}$$

For the particular case of $\varepsilon=h_0/2$ and $L=2\pi h_0$ (which then gives $|dh/dz|_{\max}=\frac{1}{2}$), the first- and second-order solutions given above are compared in Fig. 2. v_z, v_x, and dp/dz are plotted from the channel axis to the wall at an axial position of $z=L/4$ (i.e., in a converging segment of the channel). The plots are for a low applied frequency characterized by $\xi h=0.01$; i.e., the fluid-flow response is everywhere controlled by the viscous forces. Both v_x and v_z in Fig. 2 have been normalized by $3Q_z/(2h)$ (the value of $v_z^{(1)}$ in the center of the channel at dc). The pressure gradient was normalized by $3\mu Q_z/h^3$ (the value of $-\partial p^{(1)}/\partial z$ at dc).

The differences between the two levels of approximation arise completely from the fact that the pressure near the wall in a converging channel is higher (due to the "collision" with the wall) than at the center. As stated, the first-order approximation ignores this completely. The increased pressure results in an enhanced radial flux of momentum as is seen in the v_x plot. It also causes the

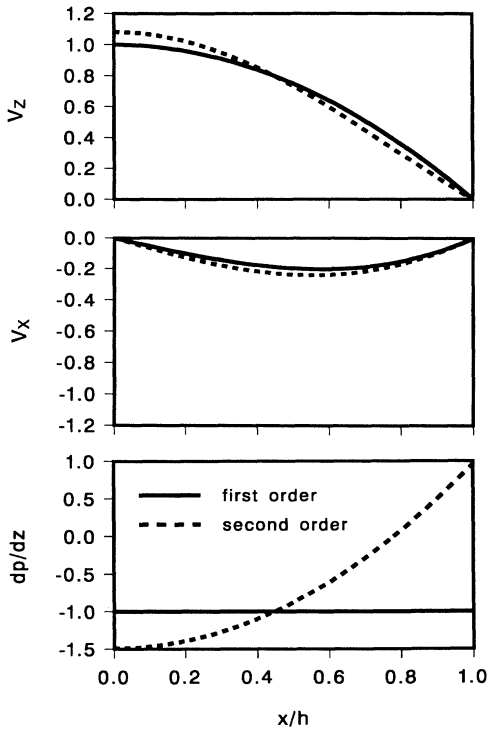

FIG. 2. Composition of the first-order and second-order solutions for the flow problem in a variable-width channel. The profiles are taken in a converging portion of the channel.

axial pressure gradient near the wall to be reduced and even reversed which, in turn, causes the axial flux of momentum near the wall to be reduced as is seen in the v_z plot.

In Fig. 3, the onset of boundary-layer flow has been investigated for the same channel geometry and axial position ($z=L/4$) as in Fig. 2. The curves have all be normalized by the same constants used in Fig. 2. Only the second-order results are displayed. It is seen that as frequency increases there develops a viscous boundary layer (i.e., a region near the wall where the velocity is reduced enough that viscous forces still dominate inertial forces). The thickness of the boundary layer is seen to be of the order ξ^{-1}, as is expected from the equations.

Now that a solution procedure has been established for flow in variable-width channels, the drag may finally be determined. In all the drag calculations to follow, the second-order results from above will be used.

C. Drag analysis

Consider the idealized (x,z) plane cross section of a porous material depicted in Fig. 4. Each periodic pore channel is assumed to be identical except for an arbitrary shift ζ_i in the z direction. There are assumed to be N pore cross sections within the averaging area. For each pore of the cross section the drag integrals are written

$$d_z^{(\text{form})}=\frac{2}{A}\int_{L_w}-pn_z\,dl \tag{52}$$

and

$$d_z^{(\text{fric})}=\frac{2\mu}{A}\int_{L_w}\left[\left[\frac{\partial v_z}{\partial x}+\frac{\partial v_x}{\partial z}\right]n_x+2\frac{\partial v_z}{\partial z}n_z\right]dl. \tag{53}$$

A is the area and L_w the length along the wall of each pore cross section. Both A and L_w are constant for all N pores. The factor of 2 denotes that both walls of a channel contribute to the drag. The length element along the wall is $dl=[1+(dh/dz)^2]^{1/2}dz$, while the (outward) normal vector to the wall is

$$(n_x,n_z)=\left[\frac{1}{[1+(dh/dz)^2]^{1/2}},\ \frac{-dh/dz}{[1+(dh/dz)^2]^{1/2}}\right]. \tag{54}$$

The form drag within the cross section is then given by

$$d_z^{(\text{form})}=\frac{1}{N}\sum_{i=1}^{N}\frac{2}{A}\int_{\zeta_i}^{L+\zeta_i}\frac{dh}{dz}p\,dz, \tag{55}$$

where the sum is over each pore comprising the cross section. Integrating by parts gives

$$d_z^{(\text{form})}=\frac{2}{AN}\sum_{i=1}^{N}\left\{h(\zeta_i)[p(L+\zeta_i)-p(\zeta_i)]-\int_{\zeta_i}^{L+\zeta_i}h\frac{\partial p}{\partial z}dz\right\}. \tag{56}$$

The second term in the brackets is independent of ζ_i, since both h and $\partial p/\partial z$ are periodic with length period L. The first term, however, depends on ζ_i. Although it is

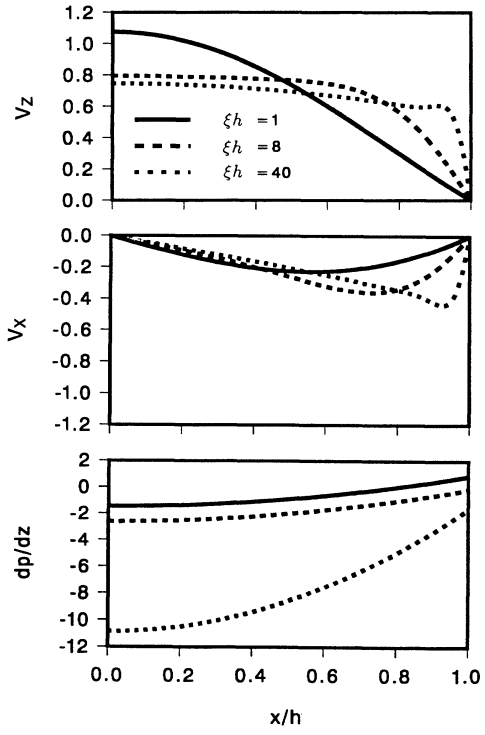

FIG. 3. The onset of boundary-layer flow. Second-order solution.

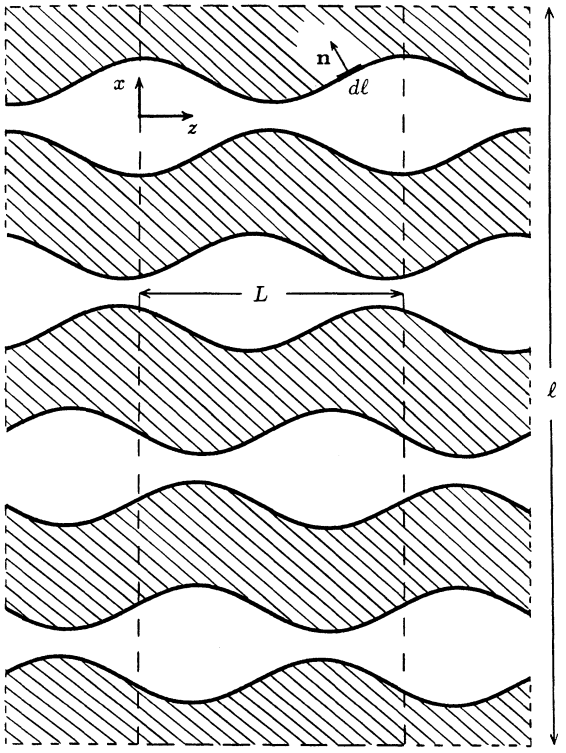

FIG. 4. A cross section of a hypothetical porous material.

true that the pressure drop $[p(L+\zeta_i)-p(\zeta_i)]$ is a constant for each of the pore cross sections and when divided by L is simply the macroscopic pressure gradient $\partial\bar{p}/\partial z$, $h(\zeta_i)$ takes on, in general, a different value for each pore. However, it will be assumed that the shifts ζ_i are uniformly distributed so that

$$\frac{1}{N}\sum_{i=1}^{N} h(\zeta_i)=h_0 \quad \left[\equiv\frac{1}{L}\int_0^L h(z)dz\right]. \tag{57}$$

The pressure gradient $\partial p/\partial z$ along the wall involved in the second term is [from Eq. (45)]

$$\frac{\partial p}{\partial z}=-i\omega\rho\dot{\bar{u}}_z-i\omega\rho\frac{Q_z}{1+hHJ}\left[\frac{F}{h}+i\xi^2h^2\frac{H}{2}\right], \tag{58}$$

so that the form drag is given by (note that $A=h_0L$)

$$d_z^{(\text{form})}=-i\omega\rho Q_z\frac{1}{h_0L}\int_0^L\frac{h_0-h(z)}{1+hHJ}\left[\frac{F}{h}+i\xi^2h^2\frac{H}{2}\right]dz. \tag{59}$$

Q_z is next replaced with the filtration velocity $\dot{\bar{w}}_z$. By definition, $\bar{w}_z$ is given by

$$\dot{\bar{w}}_z=\phi\frac{2}{A}\int_0^L dz\int_0^{h(z)}v_z dx, \tag{60}$$

$$=\frac{\phi}{h_0}Q_z, \tag{61}$$

where ϕ is the porosity represented in the cross section of Fig. 4. The form drag may now be expressed in the desired form:

$$d_z^{(\text{form})}=-i\omega\rho\gamma^{(\text{form})}\frac{\dot{\bar{w}}_z}{\phi}, \tag{62}$$

where the dimensionless complex form-drag constant $\gamma^{(\text{form})}$ is

$$\gamma^{(\text{form})}=\frac{1}{L}\int_0^L\frac{h_0-h(z)}{1+hHJ}\left[\frac{F}{h}+i\xi^2h^2\frac{H}{2}\right]dz. \tag{63}$$

The friction drag is obtained more directly since the integral of Eq. (53) is independent of ζ_i and is the same for all the pore cross sections in Fig. 4. The pertinent velocity gradients (at the wall) are

$$\frac{\partial v_z}{\partial x}=-i\xi^2\frac{Q_z}{1+hHJ}\left[G+hH\left[\frac{i\xi^2h^2}{6}-J\right]\right], \tag{64}$$

$$\frac{\partial v_z}{\partial z}=i\xi^2\frac{dh}{dz}\frac{Q_z}{1+hHJ}\left[G+hH\left[\frac{i\xi^2h^2}{6}-J\right]\right], \tag{65}$$

and

$$\frac{\partial v_x}{\partial z}=i\xi^2\frac{dh}{dz}\frac{Q_z}{1+hHJ}\left[\frac{dh}{dz}G-\frac{h\partial H/\partial z\,J}{i^{1/2}\xi\tanh i^{1/2}\xi h}\right]. \tag{66}$$

$d_z^{(\text{fric})}$ can therefore be expressed as

$$d_z^{(\text{fric})}=-i\omega\rho\gamma^{(\text{fric})}\frac{\dot{\bar{w}}_z}{\phi}, \tag{67}$$

where the complex frictional-drag constant $\gamma^{(\text{fric})}$ is

$$\gamma^{(\text{fric})}=\frac{1}{L}\int_0^L\left\{G\left[1+\left[\frac{dh}{dz}\right]^2\right]+hH\left[\frac{i\xi^2h^2}{6}-J\right]\left[1+2\left[\frac{dh}{dz}\right]^2\right]+\frac{h\partial H/\partial z\,J}{i^{1/2}\xi\tanh i^{1/2}\xi h}\frac{dh}{dz}\right\}\frac{dz}{1+hHJ}. \tag{68}$$

In general, the axial integrations of Eqs. (63) and (68) must be done numerically. The total drag coefficient γ involved in the expression for the effective fluid density [Eq. (8)] is simply $\gamma=\gamma^{(\text{form})}+\gamma^{(\text{fric})}$.

In terms of the drag coefficients, the dynamic permeability is expressed as

$$\frac{1}{k(\xi)}=\frac{i\xi^2}{\phi}(1+\gamma^{(\text{form})}+\gamma^{(\text{fric})}). \tag{69}$$

The real part of k^{-1} is related to the effective frictional resistance opposing relative flow, while the imaginary part (divided by ω) is related to the effective fluid inertia. The dc permeability k_0 is given by

$$\frac{1}{k_0}=-\frac{1}{\phi}\lim_{\xi\to 0}\xi^2(\text{Im}\{\gamma^{(\text{fric})}\}+\text{Im}\{\gamma^{(\text{form})}\}). \tag{70}$$

For the variable-channel-width model just developed, the result is

$$\frac{1}{k_0}=\frac{3}{\phi L}\int_0^L\left\{\left[1+\frac{M}{2}\right]\left[1+\left[\frac{dh}{dz}\right]^2\right]+\frac{h}{10}\frac{dh}{dz}\frac{dM}{dz}+\left[\frac{h_0}{h}-1\right]\left[1+\frac{3}{2}M\right]\right\}\frac{dz}{h^2(1+3M/10)} \tag{71}$$

where M is defined as

$$M=h\frac{d^2h}{dz^2}-4\left[\frac{dh}{dz}\right]^2. \tag{72}$$

The first two terms in the curly braces of Eq. (71) are the friction-drag contributions to the permeability, while the third term is the form-drag contribution.

So far, only the second-order results from the successive-approximation scheme have been employed. Results valid to the first order of approximation may be obtained by setting $H=0$ (and, therefore, $\partial H/\partial z=0$) in the expressions for $\gamma^{(\text{form})}$ and $\gamma^{(\text{fric})}$ and by setting $M=0$ in the expression for k_0; i.e.,

$$\gamma_{(1)}^{(\text{form})}=\frac{1}{L}\int_0^L\left[\frac{h_0}{h}-1\right]F\,dz, \tag{73}$$

$$\gamma_{(1)}^{(\text{fric})}=\frac{1}{L}\int_0^L\left[1+\left[\frac{dh}{dz}\right]^2\right]G\,dz, \tag{74}$$

and

$$\frac{1}{k_{0(1)}}=\frac{3}{\phi L}\int_0^L\left[\frac{h_0}{h^3}+\frac{1}{h^2}\left[\frac{dh}{dz}\right]^2\right]dz. \tag{75}$$

An even lower order of approximation, to be called the "zeroth-order" approximation, is made by modeling a variable-width channel as a collection of constant-width channels that are simply added in series. The drag in a constant-width channel goes as $\gamma^{(\mathrm{form})}=0$ and $\gamma^{(\mathrm{fric})}=G$. It is assumed that, in the limit, each constant-width channel has a half width $h(z)$ and a length dz. Thus, performing a sum over one length period of a variable-width channel gives the zeroth-order estimates

$$\gamma_{(0)}^{(\mathrm{form})}=0, \tag{76}$$

$$\gamma_{(0)}^{(\mathrm{fric})}=\frac{1}{L}\int_0^L G\,dz, \tag{77}$$

and

$$\frac{1}{k_{0(0)}}=\frac{3}{\phi L}\int_0^L\frac{dz}{h^2}. \tag{78}$$

The three different levels of approximation are compared in Figs. 5, 6, and 7. The three figures are plots of the real and imaginary parts of the dynamic permeability as a function of frequency for three different realizations of the pore model previously employed:

$$h(z)=h_0+\varepsilon\cos(2\pi/L).$$

The three pore models are

$$\text{model 1: } L=2\pi h_0,\quad \varepsilon=\frac{1}{2}h_0,\quad \left|\frac{dh}{dz}\right|_{\max}=\frac{1}{2};$$

$$\text{model 2: } L=2\pi h_0,\quad \varepsilon=\frac{3}{4}h_0,\quad \left|\frac{dh}{dz}\right|_{\max}=\frac{3}{4};$$

$$\text{model 3: } L=12h_0,\quad \varepsilon=\frac{3}{\pi}h_0,\quad \left|\frac{dh}{dz}\right|_{\max}=\frac{1}{2}.$$

Model 1 is the same as that used in Figs. 2 and 3.

The frequency in the figures has been normalized by the relaxation frequency ω_0 of Eq. (11). The tortuosity α_∞ required in the expression for ω_0 is defined as

$$\alpha_\infty=\lim_{\omega\to\infty}(1+\gamma^{(\mathrm{form})}) \tag{79}$$

(note that $\gamma^{(\mathrm{fric})}\to 0$ as $\omega\to\infty$ so no viscous effects are allowed for in α_∞). The tortuosity is a measure of the

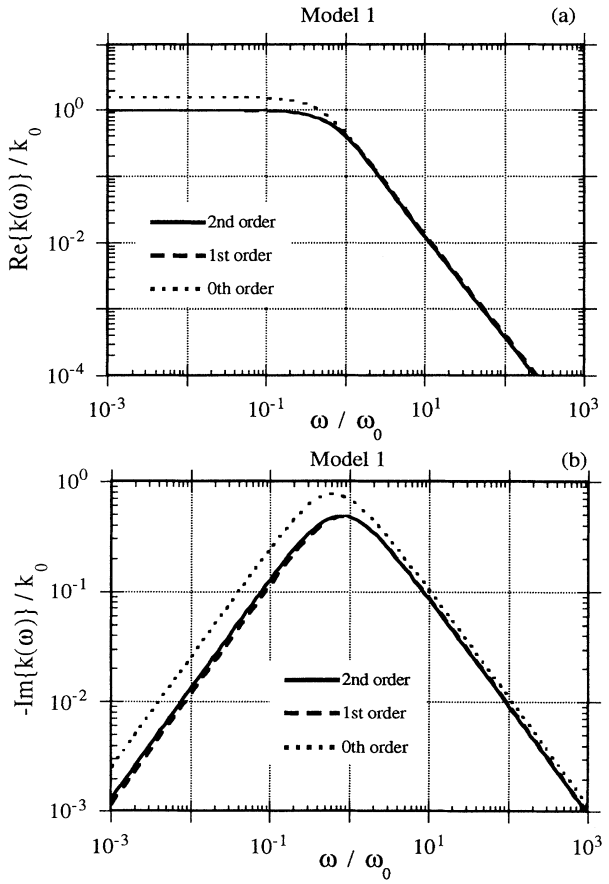

FIG. 5. Real and imaginary parts of the dynamic permeability for model 1. Comparison of second-, first-, and zeroth-order drag solutions.

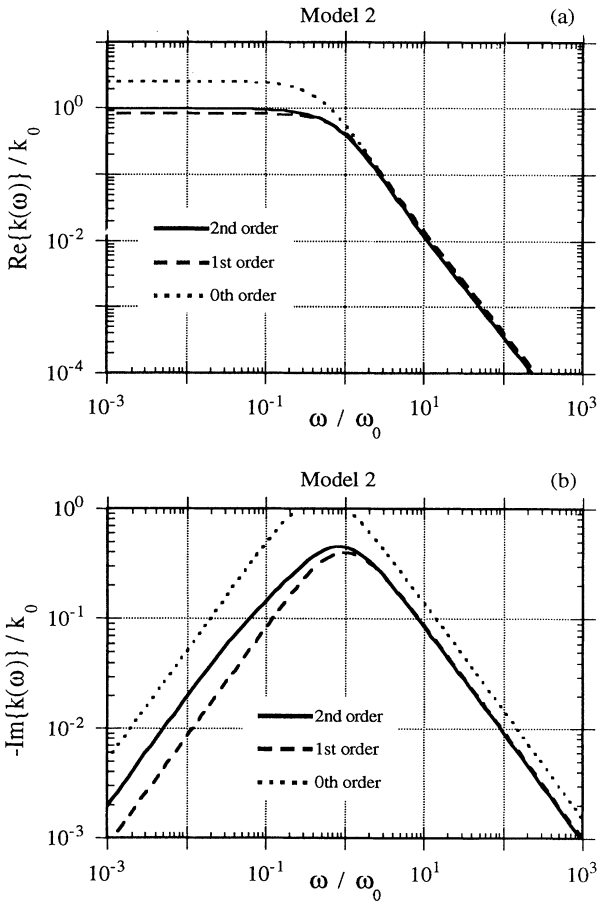

FIG. 6. Real and imaginary parts of the dynamic permeability for model 2. Comparison of second-, first-, and zeroth-order drag solutions.

enhancement in the effective fluid inertia due to pressure interactions with the pore walls. For the variable-channel-width model, α_∞ is determined from Eq. (63) to be

$$\alpha_\infty = 1 + \frac{1}{L}\int_0^L \left[\frac{h_0}{h} - 1\right]\left[\frac{1+N/2}{1+N/6}\right] dz, \tag{80}$$

where

$$N = h\frac{d^2h}{dz^2} - 2\left[\frac{dh}{dz}\right]^2. \tag{81}$$

Similarly, the dynamic permeability in each figure has been scaled by the k_0 obtained using the second-order result of Eq. (71). The difference in dc permeability estimates between the three levels of approximation is then clearly seen from the plots. For a mean half width of $h_0 = 10$ μm and a porosity of 20%, the three models give the following (second-order) results:

model 1: $\alpha_\infty = 1.15$, $k_0 = 279.8$ mD;

model 2: $\alpha_\infty = 1.51$, $k_0 = 76.0$ mD;

model 3: $\alpha_\infty = 3.37$, $k_0 = 1.1$ mD.

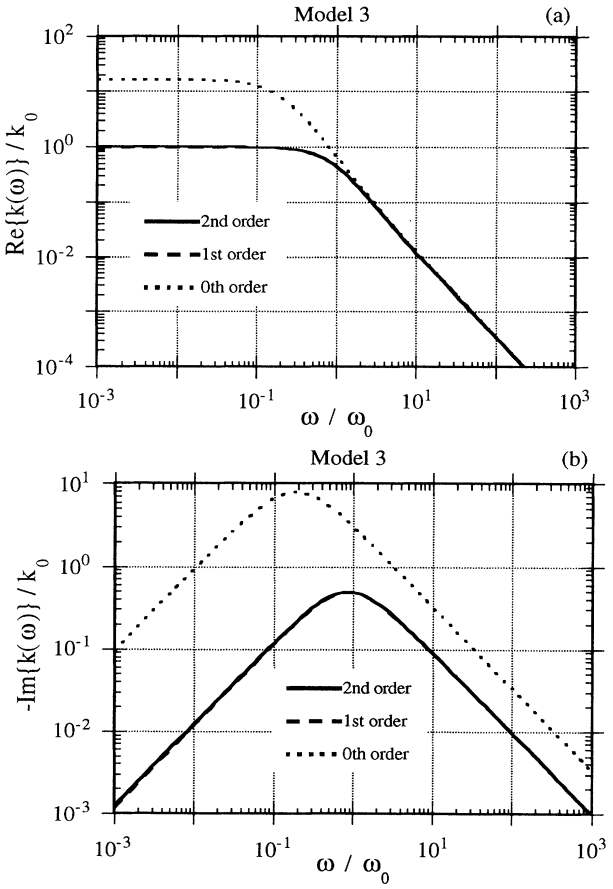

FIG. 7. Real and imaginary parts of the dynamic permeability for model 3. Comparison of second-, first-, and zeroth-order drag solutions.

Figures 5–7 show that the zeroth-order model is not very reliable and that the difference between the first-order and second-order results is only a function of the maximum channel slope. The error in the zeroth-order model is dramatically greater in model 3 as compared to model 1, even though the two models have the same maximum channel slope; however, the first- and second-order results do not vary from model 1 to model 3. In Fig. 8, the three different solutions are plotted as a function of maximum pore slope for a frequency of $\omega/\omega_0 = 0.1$. For $|dh/dz|_{\max} < 1/2$, the differences between the first-order and second-order results become negligible. The zeroth-order result only becomes valid when $|dh/dz|_{\max} < 1/5$. The error in the first-order result is proportional to $|dh/dz|^2_{\max}$, while the error in the second-order result is proportional to $|dh/dz|^4_{\max}$. Thus, for $|dh/dz|_{\max} > 3/4$ (roughly) the second-order result will also become invalid.

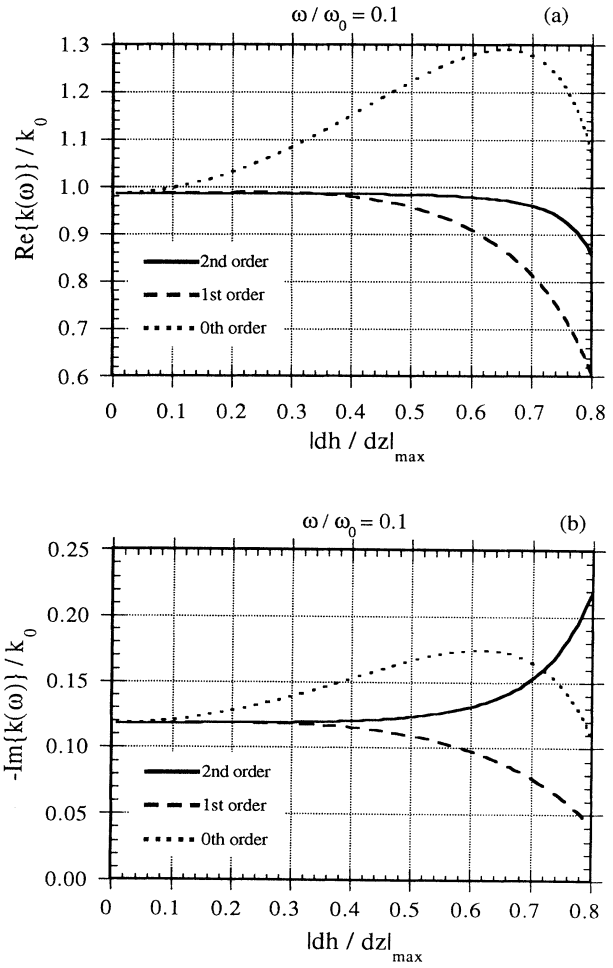

FIG. 8. Real and imaginary parts of the dynamic permeability as a function of maximum channel-wall slope at a frequency $\omega/\omega_0 = 0.1$. Comparison of second-, first-, and zeroth-order drag solutions.

D. Comparison to Biot and JKD

The second-order variable-width model is now compared to the constant-width model considered by Biot[1] and the model of Johnson, Koplik, and Dashen[8] (the "JKD" model). In the comparison, all models are required to have the same porosity and dc permeability. Again taking k_0 to be determined from the second-order results given above, one obtains that the half width h_B to be used in Biot's constant-width model is

$$h_B=\sqrt{3k_0/\phi}. \tag{82}$$

The values of $\gamma_B^{(\mathrm{form})}$ and $\gamma_B^{(\mathrm{fric})}$ corresponding to the constant-width model are obtained by setting $h(z)=h_B$ in Eqs. (63) and (68) with the result

$$\gamma_B^{(\mathrm{form})}=0, \tag{83}$$

$$\gamma_B^{(\mathrm{fric})}=G(i^{1/2}\xi h_B). \tag{84}$$

From Eq. (69) and the fact that $F=1+G$, we then have the Biot estimate of dynamic permeability k_B,

$$\frac{k_0}{k_B(\xi)}=\frac{i\xi^2h_B^2}{3}F(i^{1/2}\xi h_B). \tag{85}$$

To define the JKD model, the circular frequency ω will be employed as the independent variable instead of the inverse skin depth $\xi\ (=\sqrt{\omega\rho/\mu})$. The total drag constant γ_J for the JKD model will be expressed in terms of a complex dimensionless function $f(\omega)$ as

$$\gamma_J(\omega)=\alpha_\infty\left[1+\frac{f(\omega)}{i\omega/\omega_0}\right]-1, \tag{86}$$

where ω_0 is the transition frequency defined by Eq. (11). In terms of $f(\omega)$, the dynamic permeability $k_J(\omega)$ is written

$$\frac{k_0}{k_J(\omega)}=f(\omega)+i\frac{\omega}{\omega_0}. \tag{87}$$

The $f(\omega)$ function is defined so that (1) Darcy's law is satisfied at low-frequencies,

$$\lim_{\omega\to 0}f(\omega)=1, \tag{88}$$

and (2) ideal flow is obtained at high frequencies except for a thin viscous boundary layer of thickness ξ^{-1} near the pore walls,

$$\lim_{\omega\to\infty}f(\omega)=\left[i\frac{\omega}{\omega_0}P\right]^{1/2}, \tag{89}$$

where P is defined by Eq. (12). The argument used by JKD to define this high-frequency limit is exact and is similar to a development given by Landau and Lifshitz.[14] It provides a formal definition for $\Lambda/2$ (which is contained within P) that can be interpreted, approximately, as the pore-volume–to–pore-surface ratio. Alternatively, as mentioned in the Introduction, JKD suggest that taking

$$P\cong\tfrac{1}{2} \tag{90}$$

is an adequate approximation for many porous media. Charlaix, Kushnick, and Stokes[10] experimentally determined that Eq. (90) held (to within 10%) for their samples of lightly sintered glass beads and crushed glass. Finally, the functional nature of $f(\omega)$ is obtained by postulating a function that connects these two limits in a "simple" fashion. The function employed by JKD is

$$f_J(\omega)=\left[1+i\frac{\omega}{\omega_0}P\right]^{1/2}. \tag{91}$$

Although there is inherent nonuniqueness in defining such a function, Eq. (91) does appear to be the most simple such function.

In Figs. 9–11, the second-order results of this study are compared to the Biot and JKD results for the three pore models already considered in Figs. 5–7. In the JKD estimates, Eq. (90) was assumed, and α_∞ was taken from the second-order results. It is seen that at frequencies $\omega<\omega_0$, the imaginary part of the dynamic permeability is underestimated by both the Biot and JKD models. However, for pore slopes less than or roughly equal to 1/2, the discrepancies are negligible. In the JKD estimate, the correct behavior of the real part of $k(\omega)$ at large frequen-

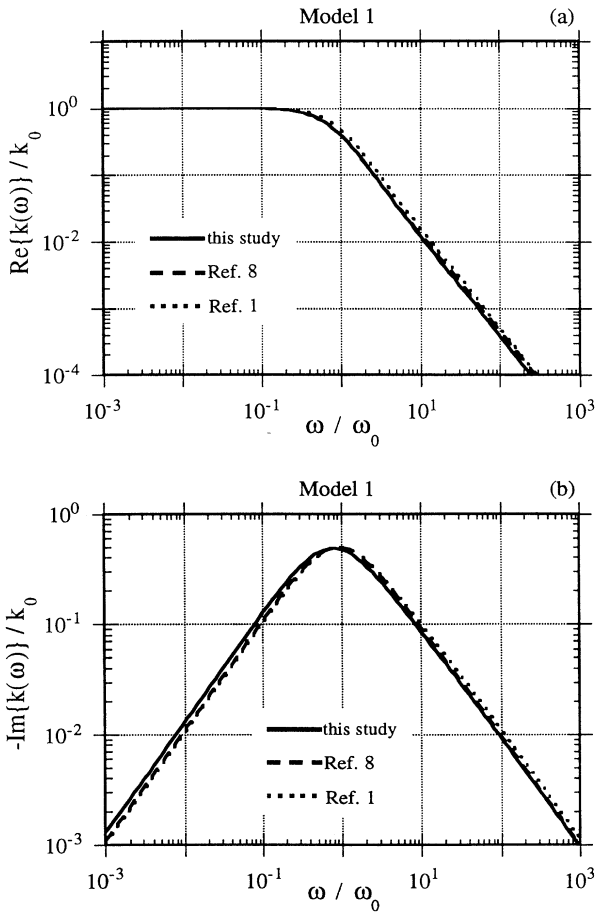

FIG. 9. Real and imaginary parts of the dynamic permeability for model 1. Comparison of second-order, JKD, and Biot drag solutions.

cies depends entirely on the value of P assumed. It was numerically determined that for all three models, Eq. (90) gave much better results than interpreting $\Lambda/2$ in Eq. (12) to be the pore-volume to pore-surface ratio. In Fig. 12, the Biot, JKD, and second-order results are compared as a function of maximum channel-wall slope at the same frequency considered in Fig. 9 ($\omega/\omega_0=0.1$). It is seen that for slopes above roughly 0.6, the JKD model begins to break down.

E. Modified JKD model

The JKD model can be modified so as to match the low-frequency behavior exactly. This is done by requiring the $f(\omega)$ function to satisfy the exact limit

$$\lim_{\omega\to 0} f(\omega)=1+i\frac{\omega}{\omega_0}\beta, \tag{92}$$

where the parameter β depends on the low-frequency real parts of $\gamma^{(\text{form})}$ and $\gamma^{(\text{fric})}$ as

$$\beta=\frac{1}{\alpha_\infty}\left[1+\lim_{\omega\to 0}\mathrm{Re}\{\gamma^{(\text{form})}\}+\lim_{\omega\to 0}\mathrm{Re}\{\gamma^{(\text{fric})}\}\right]-1. \tag{93}$$

The parameter β is a measure of the effective fluid-inertia enhancement at low frequencies; however, we note that unlike α_∞, viscous forces affect its value. Recall that at low frequencies, JKD only require that $f(0)=1$.

There are an infinity of $f(\omega)$ functions that can connect the high-frequency and low-frequency limits [the high-frequency limit is still given by Eq. (89)]. Five such possible functions are

$$f_1(x)=1-\frac{P}{2\beta}+\frac{P}{2\beta}\left[1+ix\frac{4\beta^2}{P^2}\right]^{1/2}, \tag{94}$$

$$f_2(x)=\frac{1+ixa}{(1+ixa^2)^{1/2}}, \tag{95}$$

$$f_3(x)=\frac{1+(ix)^{1/2}a+ixa}{1+(ix)^{1/2}a}, \tag{96}$$

$$f_4(x)=1-\frac{P}{3\beta}+\frac{(ix)^{1/2}}{\tanh[(ix)^{1/2}3\beta/P]}, \tag{97}$$

$$f_5(x)=1-\frac{P}{2\beta}+(ix)^{1/2}\frac{I_0[(ix)^{1/2}4\beta/P]}{I_1[(ix)^{1/2}4\beta/P]}, \tag{98}$$

where the frequency has been rescaled as

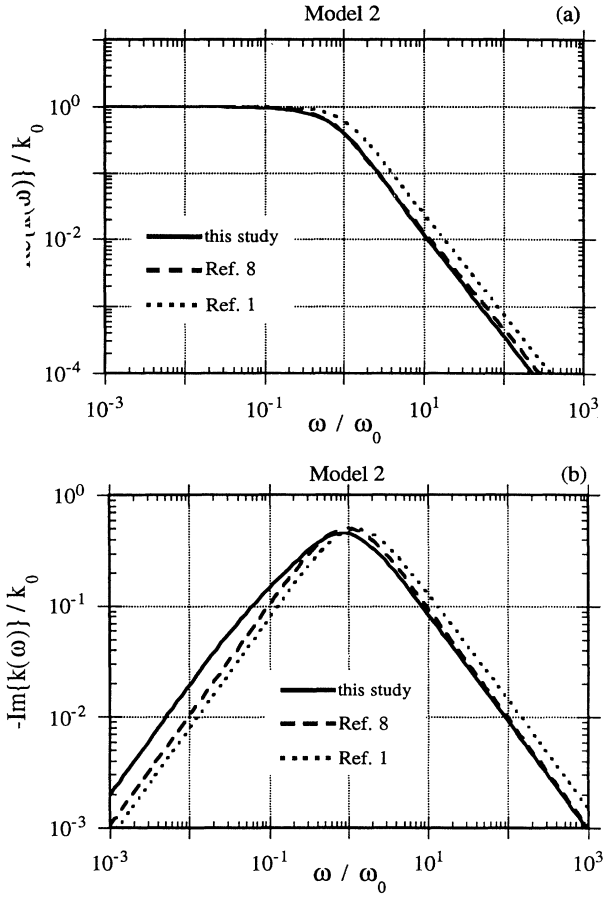

FIG. 10. Real and imaginary parts of the dynamic permeability for model 2. Comparison of second-order, JKD, and Biot drag solutions.

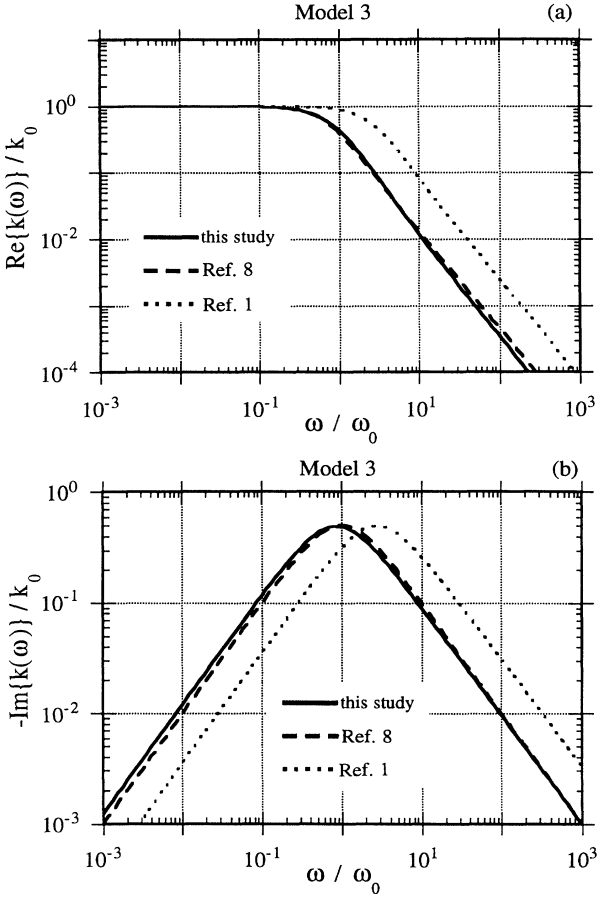

FIG. 11. Real and imaginary parts of the dynamic permeability for model 3. Comparison of second-order, JKD, and Biot drag solutions.

$$x = \omega P/\omega_0, \tag{99}$$

the parameter a is defined

$$a = 1 - \left[1 - \frac{2\beta}{P}\right]^{1/2}, \tag{100}$$

and I_0 and I_1 are modified Bessel functions of the first kind. We can reject f_4 and f_5 as being too difficult to numerically calculate as compared to the others.

With frequency a real variable, each of these functions has nearly identical frequency dependence. However, if analysis is extended into the complex ω plane (as is convenient—but not necessary—when returning to the time domain via the inverse-Fourier transform), each of these functions has different behavior off the real axis. Johnson, Koplik, and Dashen[8] demonstrate that the zeros and singularities of $k(\omega)$ must lie on the positive imaginary axis (note that we employ an $e^{i\omega t}$ time dependence, while JKD employ the more common $e^{-i\omega t}$). The singularities present no problems in the inverse-Fourier transform so long as analysis is restricted to the lower-half ω plane as is usual [note that $k(\omega)$ is exponentially unbounded as $\mathrm{Im}\{\omega\}$ extends to positive infinity because of the $e^{i\omega t}$ time dependence and causality]. Indeed, from a computational standpoint, all that is needed is that the zeros and singularities of $k(\omega)$ lie in the upper-half ω plane and not necessarily on the positive-imaginary axis.

All of the $f(\omega)$ functions given above can lead to $k(\omega)$ singularities in both the upper-half and lower-half planes. However, the following combination never has zeros or singularities in the lower-half plane,

$$\frac{k_0}{k(x)} = \begin{cases} f_1(x) + ix/P, & P \le 2\beta \\ f_2(x) + ix/P, & P \ge 2\beta. \end{cases} \tag{101}$$

When $P = 2\beta$, the JKD estimate is recovered. Clearly, $2\beta/P$ is a fundamental material property controlling the frequency dependence of the dynamic permeability.

Although the definition of β given by Eq. (93) is exact, it requires knowledge of how the real parts of the drag coefficients behave at low frequencies. It is possible that such information is only obtainable by solving the time-harmonic viscous-flow problem for each porous material type that is considered. For the variable-width model, these low-frequency limits are obtained from Eqs. (63) and (68) as

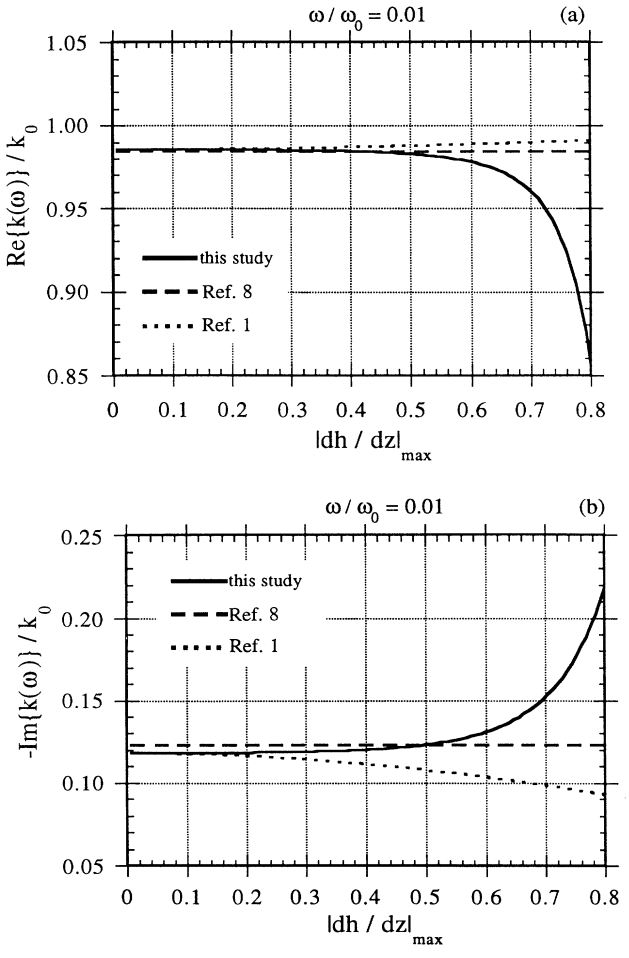

FIG. 12. Real and imaginary parts of the dynamic permeability as a function of maximum channel-wall slope at a frequency $\omega/\omega_0 = 0.1$. Comparison of second-order, JKD, and Biot drag solutions.

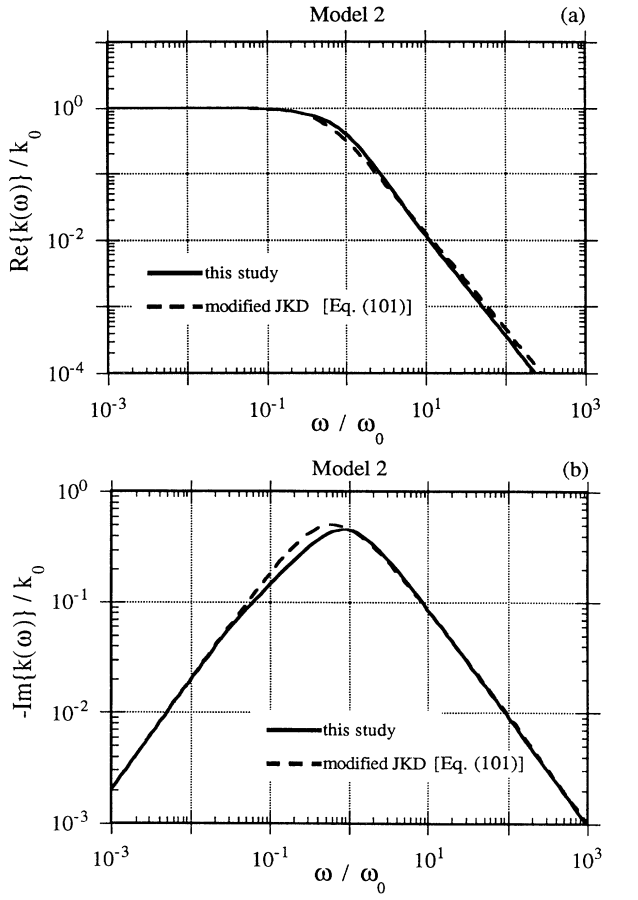

FIG. 13. Real and imaginary parts of the dynamic permeability for model 2. Comparison of the second-order and modified JKD drag solutions.

$$\lim_{\xi\to 0}\mathrm{Re}\{\gamma^{(\mathrm{form})}\}=\frac{6}{5L}\int_0^L\left[\frac{h_0}{h}-1\right]\left[1+\frac{N}{2}+\frac{1}{2}\left[\frac{1+3M/2}{1+3M/10}\right]\left[\frac{4M}{7}-\frac{N}{5}\right]\right]\frac{dz}{1+3M/10} \tag{102}$$

and

$$\lim_{\xi\to 0}\mathrm{Re}\{\gamma^{(\mathrm{fric})}\}=\frac{1}{5L}\int_0^L\frac{dz}{1+3M/10}\left[1+\left[\frac{dh}{dz}\right]^2-\left[\frac{3M}{2}-N\right]\left[1+2\left[\frac{dh}{dz}\right]^2\right]\right.$$
$$+\frac{dh}{dz}\left[\frac{1}{14}\left[5M\frac{dh}{dz}-h\frac{dM}{dz}\right]-\frac{1}{5}\left[3N\frac{dh}{dz}-h\frac{dN}{dz}\right]\right]$$
$$\left.+3\left[\frac{4M/7-N/5}{1+3M/10}\right]\left\{\left[1+\frac{M}{2}\right]\left[1+\left[\frac{dh}{dz}\right]^2\right]+\frac{h}{10}\frac{dh}{dz}\frac{dM}{dz}\right\}\right]. \tag{103}$$

These rather cumbersome expressions do not appear to relate in any simple manner to the definitions of α_∞ and k_0 given by Eqs. (80) and (71).

In Fig. 13, the "modified" JKD estimate based on Eq. (101) is compared to the second-order results of this study for the same model 2 considered earlier. Although the modified JKD estimate is required to have the correct behavior in both the limits of high and low frequencies, it still has some trouble mimicking the behavior near the transition frequency with maximum discrepancies of about 40%. Some of this discrepancy could be due to our own second-order results beginning to break down. However, for channel slopes less than or roughly equal to 1/2, the modified JKD estimate becomes essentially exact. The values of β obtained for the three pore models discussed earlier are model 1 $\beta=0.296$, model 2 $\beta=0.956$, and model 3 $\beta=0.225$. Thus, with $P=1/2$, it is seen that 2β can be both greater than and less than P.

F. Generalizing the variable-width model to three dimensions

The variable-width model presented so far has been limited to two-dimensional flow channels all aligned in the same direction. Adjustments can be made to extend the model, in an approximate manner, to three-dimensional isotropic media. First, it may be assumed that in an isotropic medium supporting compressional-wave propagation in a particular direction, roughly one third of the pore space will be involved in the conduction of relative flow. This one third of the pore space is modeled as a collection of variable-width channels aligned in the direction of wave propagation. The remaining two thirds of the pore space can be thought to consist of flow channels aligned perpendicular to the wave direction and, therefore, not involved in the flow. Because the average relative flow $\tilde{\mathbf{w}}$ will be reduced by a factor of 3 in such an isotropic model, the drag results given above should be modified by replacing $1+\gamma$ in Eq. (8) by $3(1+\gamma)$. This allows $\tilde{\mathbf{w}}$ to be interpreted as a filtration velocity as in Darcy's law. It also means that the tortuosity α_∞ will be enhanced by a factor of 3, while the dc permeability will be reduced by a factor of 3.

If it is desired to model the channels as having circular cross sections as opposed to the planar cross sections considered so far, one must simply make the substitution

$$\tanh[i^{1/2}\xi h(z)]\to\frac{I_1[i^{1/2}\xi a(z)]}{I_0[i^{1/2}\xi a(z)]}, \tag{104}$$

in the above expressions for $\gamma^{(\mathrm{form})}$ and $\gamma^{(\mathrm{fric})}$ [Eqs. (63) and (68)], where again I_1 and I_0 are modified Bessel functions of the first kind and $a(z)$ is the pore-radius function. This substitution is determined by carrying out the flow modeling in cylindrical coordinates. Of course, such a replacement will affect the high- and low-frequency limits used to define k_0, a_∞, and Eqs. (102) and (103).

IV. CONCLUSIONS

A model has been presented that determines the drag force in porous-material models that possess variable-width flow channels. The flow channels are assumed to have widths that vary smoothly, a periodicity L that is at least a factor of 4 greater than the mean channel half width, and maximum channel-wall slopes that are less than or equal to 3/4. The dynamic permeability determined from such a model has been compared to the dynamic permeability predictions of Biot[1] and Johnson, Koplik, and Dashen.[8] It has been shown that for maximum channel-wall slopes less than 1/2, the JKD model is very good. The Biot model is less adequate, particularly if large tortuosities are present (as in model 3). The JKD model has also been modified so that it is guaranteed to have the correct behavior in the limit of small frequencies (the existing JKD model is already accurate in the limit of high frequencies). It was also shown that a simple series sum of constant-channel-width flow resistances does a poor job in approximating the drag in variable-width channels. This is because form drag is neglected in such a model.

[1]M. A. Biot, J. Acoust. Soc. Am. **28**, 179 (1956).
[2]A. Bedford, R. D. Costley, and M. Stern, J. Acoust. Soc. Am. **76**, 1804 (1984).
[3]T. Yamamoto and A. Turgot, J. Acoust. Soc. Am. **83**, 1744 (1988).
[4]S. R. Pride, A. F. Gangi, and F. D. Morgan, J. Acoust. Soc. Am. **92**, 3278 (1992).
[5]M. A. Biot and D. G. Willis, J. Appl. Mech. **24**, 594 (1957).
[6]M. A. Biot, J. Acoust. Soc. Am. **28**, 168 (1956).
[7]M. A. Biot, J. Appl. Phys. **33**, 1482 (1962).
[8]D. L. Johnson, J. Koplik, and R. Dashen, J. Fluid Mech. **176**, 379 (1987).
[9]R. J. S. Brown, Geophys. **45**, 1269 (1980).
[10]E. Charlaix, A. P. Kushnick, and J. P. Stokes, Phys. Rev. Lett. **61**, 1595 (1988).
[11]M. Zhou and P. Sheng, Phys. Rev. B **39**, 12 027 (1989).
[12]G. K. Batchelor, *Fluid Dynamics* (Cambridge University Press, Cambridge, England, 1967).
[13]W. F. Murphy, K. W. Winkler, and R. L. Kleinberg, Geophys. **51**, 757 (1987).
[14]L. D. Landau and E. M. Lifshitz, *Fluid Mechanics,* 2nd ed. (Pergamon, New York, 1987), Sec. 24.